MATERIALS SCIENCE

The genesis of citrated ultrathin hydroxyapatite nanorods

Yuqi Wang[1]†, Su Yan[1]†, Xinyu Tan[2]†, Ethan Gerhard[1], Hui Xu[1], Haiyue Jiang[3], Jian Yang[4,5,6]*

Ideal orthopedic biomaterials should replicate both the hierarchical structure and exceptional mechanical strength of natural bone. Traditional polymer-hydroxyapatite composites, typically limited up to 40 wt % hydroxyapatite, offer only modest mechanical improvements. Efforts to enhance strength by using stiffer polymers have largely failed, as increased polymer stiffness does not translate to improved composite mechanics. In contrast, natural bone's load-bearing capability arises from the synergy between citrate, soft collagen, and ultrathin hydroxyapatite nanocrystals (~3 nanometers). Here, we show that elastic poly(octamethylene citrate) enables up to 60 wt % hydroxyapatite incorporation, mimicking the bone's mineral content. Through a top-down "citrification" process and hot pressing, hydroxyapatite microparticles are partially dissolved and recrystallized into superthin (~5 nanometers) nanorods, enhancing organic-inorganic integration and replicating bone's Ca/P ratios and architecture. The resulting composites exhibit compressive strengths exceeding 250 megapascals, unprecedented in polymer-mineral systems, offering a molecular design strategy for next-generation load-bearing orthopedic implants.

INTRODUCTION

Effective bone regeneration demands biomaterials that not only replicate the hierarchical architecture of native bone but also match its mechanical and biological performance. Traditionally, efforts to improve hydroxyapatite (HA) composite strength have focused on increasing polymer matrix stiffness. However, these approaches yield only modest gains, typically a two- to threefold increase over the base polymer, and fail to match the load-bearing strength of natural bone (*1*–*5*). For example, even with highly rigid polymers like poly(lactic acid) (PLA) and polymethylmethacrylate (PMMA), widely used in bone cements, the incorporation of 15 to 40 wt % HA yields only limited gains in compressive strength [increase in ~1.8-fold in PLA (*5*), from ~110 to 120 MPa in PMMA (*6*)]. Moreover, most of these materials also remain biological inert and lack intrinsic osteoinductive or osteoconductive properties (tables S1 and S2).

Counterintuitively, natural bone achieves mechanical strengths of 150 to 300 MPa and high toughness through its hierarchical structure composed of ultrathin HA nanorods (2 to 4 nm thick, ~100 nm long) embedded within a soft collagen matrix (*7*–*16*). These nanostructures help bones resist crack propagation and are organized with precision (*17*, *18*). However, fabricating synthetic composites with sub–10-nm HA nanorods remains a major challenge. While bottom-up approaches in natural bone can yield ultrathin HA in collagen scaffolds, there are few reports of polymer-HA composites that replicate the mineral phase dimensions and mechanical strength of native bone (*10*, *13*, *19*–*21*). A key component to bone's structure and function is citrate, a small molecule accounting for ~5% of bone's organic content, predominantly found on the surfaces and in between the platelet structures of apatite crystals in a form of octacalcium phosphate citrate (OCP-citrate) (*9*, *22*). Citrate not only inhibits lateral HA growth and promotes elongation along the *c* axis but also enhances HA-collagen interactions, enabling strong organic-inorganic integration crucial for bone's mechanical integrity (*10*, *18*, *23*).

Inspired by this, we developed a citrate-based polymer, poly (octamethylene citrate) (POC), to engineer HA composites that emulate bone's structure and mechanics, surpassing the conventional polymer-HA systems. Notably, POC-based orthopedic implants including interference screws, suture anchors, and bone void fillers marked a substantial milestone in modern biomaterials science as POC joins only a handful of biodegradable synthetic polymers ever authorized by Food and Drug Administration (FDA) for human uses (*24*). We have previously found that citrate plays critical roles in orchestrating bone regeneration through metabonegenic regulation. Human mesenchymal stem cells (hMSCs) showed robust proliferation and differentiation on citrate-based composites, which underscores the promise of citrate-based materials as a generation of biomaterial (*25*–*31*), setting it apart from conventional stiff polymers like poly (lactic-*co*-glycolic acid) (PLGA). In traditional composites, HA is mixed with polymers like PLGA at less than 40 wt %, yielding compressive strengths around 30 to 50 MPa and modulus around 120 MPa (*4*, *32*). In contrast, we found that POC can incorporate up to 60 wt % HA, similar to bone mineral content, while maintaining elasticity (*33*, *34*). This boosts composite compressive strength to 250 to 280 MPa and modulus to ~500 to 800 MPa, representing more than a 500-fold increase over pure POC (0.5-MPa strength, ~1-MPa modulus) (fig. S2A and tables S1 and S2) (*35*). While the modulus of POCHA is lower than that of mature cortical bone, its compressive strength falls within the range of natural bone to support its applications in load-bearing scenarios. Also, its modulus closely matches that of cancellous bone and regenerating cortical bone, which typically lies between 0.1 and 2 GPa (*36*, *37*), supporting POCHA as load-sharing and biomimicry bone regenerative implants. However, much like the elusive mechanism by which nature combines soft, elastic collagen and apatite to form bone tissue, the process through which soft and elastic POC contributes to the

[1]Department of Biomedical Engineering, The Pennsylvania State University, University Park, PA 16802, USA. [2]Department of Traumatic Surgery, Center for Orthopaedic Surgery, The Third Affiliated Hospital of Southern Medical University, Guangdong 510630, P.R. China. [3]Plastic Surgery Hospital, Chinese Academy of Medical Sciences and Peking Union Medical College, Beijing 100144, P.R. China. [4]Department of Materials Science and Engineering, School of Engineering, Westlake University, Hangzhou, Zhejiang 310030, P.R. China. [5]Research Center for Industries of the Future, Westlake University, Hangzhou, Zhejiang 310030, P.R. China. [6]Center for Biobased Materials, Muyuan Laboratory, Zhengzhou, Henan Province 450016, P.R. China.
*Corresponding author. Email: yangjian07@westlake.edu.cn
†These authors contributed equally to this work.

formation of ultrastrong POC-HA composites remains poorly understood.

Here, we reveal that POC induces a top-down transformation of HA microparticles into ultrathin, needle-like nanorods (~5 nm thick, ~115 nm long) through a "citrification" process. This mimics the natural function of citrate by exposing binding sites, partially dissolving HA, and guiding directional recrystallization during hot pressing. The resulting structure closely mirrors that of bone, with aligned nanorods, blurred organic-inorganic boundaries, and biomimetic aspect ratios. Citrification not only enhances organic-inorganic bonding but also replicates key biochemical features of bone, including Ca/P ratios and intermolecular interactions. The resulting POC-HA composites display exceptional compressive strength and bioactivity, supporting osteoblast viability and mineralization. These findings present a paradigm in biomaterials design, leveraging a naturally inspired molecular strategy to construct bone-mimetic, load-bearing composites with both structural and functional fidelity.

RESULTS

POC enabled citrification of HA

The citrification process initiated by kneading POC oligomer with HA microparticles, partially dissolved microparticles and generated ion-rich baths that blur the boundaries between organic and inorganic phases (Fig. 1A). Uncrosslinked POC60HA (UPOC60HA) already exhibited greater compressive strength and elasticity than untreated PLGA60HA (UPLGA60HA) (Fig. 1B and fig. S2, B and C). The carboxylic groups of POC gradually dehydroxylated HA, which was examined using attenuated total reflection Fourier–transform infrared (ATR-FTIR) spectroscopy. Hydroxylation levels are expected to inversely correlate with the full width at half maximum (FWHM) of the 960 cm^{-1} peak (PO_4^{3-}) (*38*). The broader peak in UPOC60HA, compared to UPLGA60HA and the HA reference, highlighted the strong dehydration capacity of the POC (dissolved particles in Fig. 1, A and C). In addition, POC incorporation caused a redshift in the characteristic apatitic phosphate at 1020 to 1010 cm^{-1}, a shift observed exclusively in UPOC60HA composites, reflecting alternations in the local chemical environment surrounding the phosphate groups (*39*). In natural bone, the presence of multiple reactive inorganic phases reduces hydroxylation levels, leading to decreased crystal size and greater structural disorder (*40*). Dehydroxylation of HA further facilitated the phosphate transformation into acidic phosphate, as evidenced by an increased area percentage of 885 cm^{-1} peak, which was more pronounced in UPOC60HA than in UPLGA (*41*–*43*).

The hydrogen phosphate was further identified as monetite by x-ray diffraction (XRD) by its characteristic peaks, especially (020) ($2\Theta = 26.57°$) and (−112) ($2\Theta = 30.19°$) (Fig. 1D and fig. S2D) (*44*, *45*). Furthermore, FTIR analysis revealed a blueshift in the carbonyl stretching peak, shifting from 1726 to 1732 cm^{-1} in UPOC60HA and from 1745 to 1755 cm^{-1} in UPLGA60HA, suggesting interactions between carbonyl groups and electron-withdrawing species, such as phosphate. The interactions between carboxylates and calcium (Ca) ions were characterized by the emergence of shoulder at ~1600 cm^{-1}, indicating the formation of ionic bonds between polymeric networks and HA (Fig. 1E) (*46*). Collectively, FTIR and XRD analyses suggested that both POC and PLGA treatment partially dissolved HA by reducing the crystallinity and crystal size, with a more pronounced effect in UPOC60HA (fig. S2E and tables S3 and S4).

Similar findings were also observed when composited HA microparticles with citrate (fig. S1, F to H). These findings demonstrated the necessity of dehydroxylating HA to expose binding sites for better organic-inorganic integration. They highlight the superior transformative capability of POC, compared to PLGA, in modulating HA

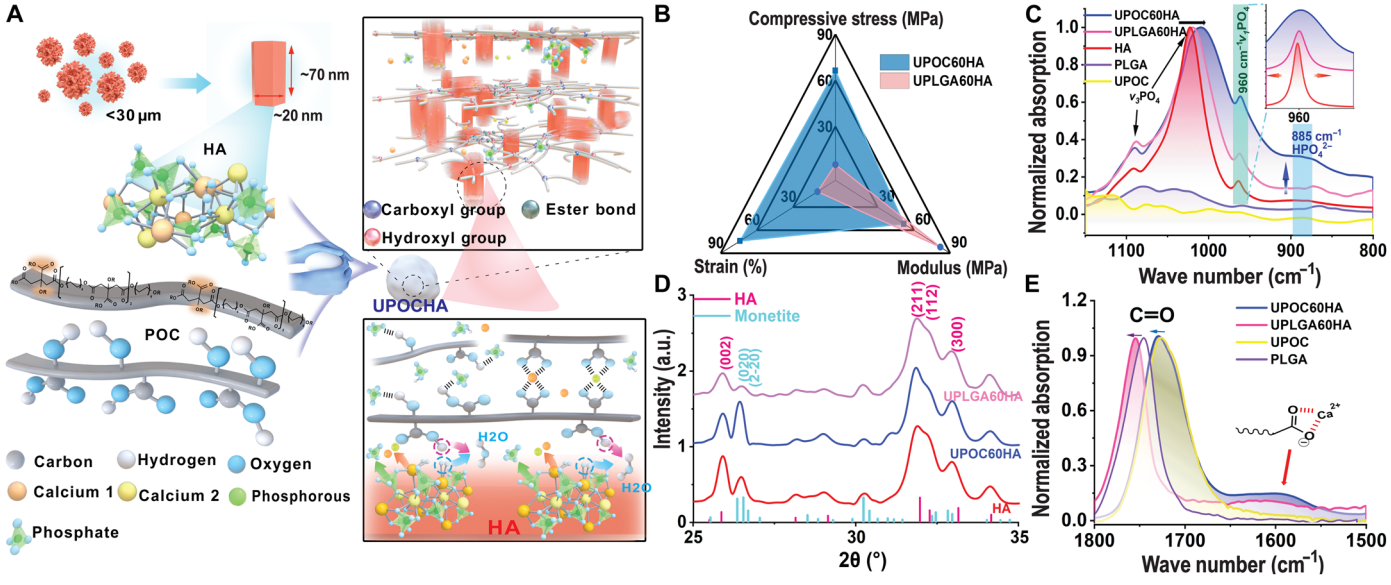

Fig. 1. Dehydroxylation and creation of ionic bath on HA microparticles by citrification. (**A**) Schemic demonstration of fabrication of UPOCHA composites and the dissolution of HA microparticles (blurry HA rods) within the polymer networks with the hypothesized chemical bonding between HA and POC; reaction between POC and HA releases water as dehydroxylation which is followed by release of calcium and phosphate into polymeric matrix. (**B**) Comparison of modulus versus compressive stress versus strain for UPOC60HA and UPLGA60HA. (**C**) FTIR spectra of HA, UPOC, PLGA, UPOC60HA, and UPLGA60HA focusing on the phosphate bonds. The arrows show the shifts of the corresponding peaks. (**D**) XRD spectra of HA, UPLGA60HA, and UPOC60HA with JCPDS identity on the bottom. (**E**) FTIR spectra of PLGA, UPOC, UPOC60HA, and UPLGA60HA, focusing on carbonyl groups. The arrows indicating the shifts of corresponding peaks, and carboxylate chelation on Ca ions is assigned to the shoulder at ~1600 cm^{-1}. a.u., arbitrary units.

structure. POC not only initiated citrification of HA by dehydroxylation but also facilitates the formation of an ion-rich environment, thereby improving the integration of polymer matrix and inorganic minerals for enhanced mechanical performance.

Hot pressing facilitated directional recrystallization and biomimicry apatite

To further enhance cross-linking and mechanical strength, UPOC60HA underwent hot pressing, resulting in thermally crosslinked and compressed POC60HA (CPOC60HA). The mechanical properties of CPOC60HA were at least five times greater than those of compressed UPLGA60HA (CPLGA60HA) (fig. S3, A to C). Recrystallization was observed in both CPOC60HA and CPLGA60HA, as indicated by increased intensity of the (002) diffraction peak in HA, although still lower than that of the HA reference, and decreased intensity of the (020) peak corresponding to monetite. In addition, hot pressing partially restored HA crystallinity and hydroxylation (fig. S3, D to F, and tables S3 and S4). These XRD results suggest that HA recrystallization likely originated from released free ions and intermediate inorganic phases generated by UPOC under hot pressing.

We conducted scanning transmission electron microscopy (STEM) to examine the nanostructure changes in HA microparticles (Fig. 2, A and B). STEM images of UPLGA60HA (Fig. 2C) and UPOC60HA (Fig. 2D) revealed the transformation of HA microparticles into less distinct structures, more prominently in UPOC60HA, indicating the better dissolution of HA by POC and the presence of intermediate mineral phases. This transformation contributed to improved HA integration within the polymeric matrix, as evidenced by the blurred boundary between organic and inorganic phases in UPOC60HA (marked by red line in Fig. 2F), compared to the distinct interfaces observed in UPLGA60HA and HA reference (Fig. 2E). The selected area showed (211) ($d = 2.82$ Å) and (202) ($d = 2.63$ Å) reflections which further confirmed the identity of HA, validating the superior integration of POC-HA composites compared to PLGA-HA (Fig. 2F).

Hot pressing induced directional recrystallization of HA fiber in both CPLGA60HA (Fig. 2G) and CPOC60HA (Fig. 2H). At higher magnification, CPOC60HA revealed nanorods that were markedly smaller, denser, and more uniformly distributed compared to those in CPLGA60HA. This refinement in nanostructure can be attributed to the abundant ionic environment and stronger organic-inorganic interactions provided by the POC matrix, which facilitated directional recrystallization. The ultrathin nanorods reappeared with well-defined boundaries and a homogeneous dispersion throughout the polymer network, in contrast to the thick structures observed in CPLGA60HA composites (Fig. 2, I and J). Using fast Fourier transform (FFT), we defined the (002) plane ($d = 3.47$ Å) and (100) plane ($d = 8.12$ Å) in HA fibers as length and width, respectively (Fig. 2J).

Figure 3A schematically demonstrated the transformation of HA into nanorods under hot pressing and POC facilitation. Similarly, STEM analysis of sheep cortical bone also revealed a homogeneous and highly organized network of ultrathin, fiber-like nanostructures. As shown in Fig. 3B, these structures are consistently aligned and measure ~4 nm in thickness. At a larger magnification (Fig. 3C), a distinct lamellar architecture emerges, characterized by alternating dark and light contrasts, reflecting phase heterogeneity within the bone matrix. FFT analysis of the ordered regions (Fig. 3D) reveals multiple reflections with d-spacings of 3.43, 3.88, and 2.8 Å, corresponding to (002), (111), and (211) lattice planes, respectively, confirming the presence of HA nanocrystals. In contrast, less organized regions (Fig. 3E) exhibit weaker (002) reflections and a d-spacing of ~2.86 Å, indicative of amorphous calcium phosphate (*47*, *48*). Hot pressing combined with POC-enabled HA citrification transformed HA microparticles into nanorods ~5 nm thick and 115 nm long, closely mimicking native apatite morphology. This ultrathin structure, rarely achieved in synthetic composites, likely underpins the exceptional mechanical strength of CPOC60HA. Analysis of length-to-width ratios from STEM images revealed elongation along the [002] direction and refinement along the [100] direction in both CPLGA60HA and CPOC60HA, but the biomimicry effect was more pronounced upon POC treatment (Fig. 3F and fig. S3G).

Hot pressing–induced recrystallization elicited a pronounced reorganization of the HA lattice within the CPOC60HA composite. Notably, the diffraction intensity corresponding to the (100) reflection was substantially diminished relative to pristine HA microparticles and the UPOC60HA counterpart, converging toward the diffraction profile characteristic of natural sheep femur (Fig. 3G). In parallel, a marked amplification of the (002) reflection was observed in CPOC60HA following thermal consolidation (Fig. 3H), indicative of preferential crystal growth along the *c* axis, consistent with the findings in STEM observations. Quantitative evaluation of the (002)/(100) intensity ratio confirmed the emergence of a biomimetic HA morphology characterized by elongated nanofibrous crystallites with enhanced aspect ratios, particularly in the POC-treated composite compared to the PLGA counterpart. (Fig. 3I and fig. S3H). Such lattice organization, closely mirroring that of native bone mineral, is expected to improve load-bearing performance by facilitating efficient stress transfer while suppressing crack initiation and propagation, thereby imparting superior fracture toughness. Together, these findings highlighted the unique role of POC in orchestrating mineral reorganization into bone-like architectures, a capability absent in conventional polymer matrices.

Collectively, thermal compression facilitated the recrystallization of HA into nanorods, as the strong binding interactions of POC suppressed crystallization of phosphate and calcium ions along the *a* planes (parallel to the *c* axis). This confinement effectively controlled crystal thickness, closely resembling the regulatory role of citrate in natural bone. As a result, the POCHA composites not only share the chemical features of native bone, composed of mixtures of calcium phosphate, but also successfully replicate the morphology of bone apatite fibers, thereby achieving both compositional and structural biomimicry.

Biomimetic mineral chemistry of recrystallized HA

Figure 4A demonstrates a homogeneous distribution of organic and inorganic phases, as carbon signals, indicative of extracellular matrix components like collagen and citrate, perfectly align with calcium (Ca) and phosphorus (P) signals in energy-dispersive x-ray spectroscopy (EDS) elemental mapping. This analysis also confirmed the recrystallization of HA nanorods embedded in the crosslinked POC matrix, supporting a well-integrated organic-inorganic structure. Notably, discrete Ca and P signals (marked by red and green arrows, respectively) contrasted with the continuous signals in HA reference, suggesting ion release and Ca/phosphate chelation by POC. The resulting chemical environment closely resembles that of natural bone, reinforcing the biomimetic nature of CPOC60HA (Fig. 4, A to C). Moreover, POC incorporation increased the Ca/P ratio from 1.67 to 2.06 in UPOC60HA, with a lesser effect in UPLGA60HA (fig. S4, A

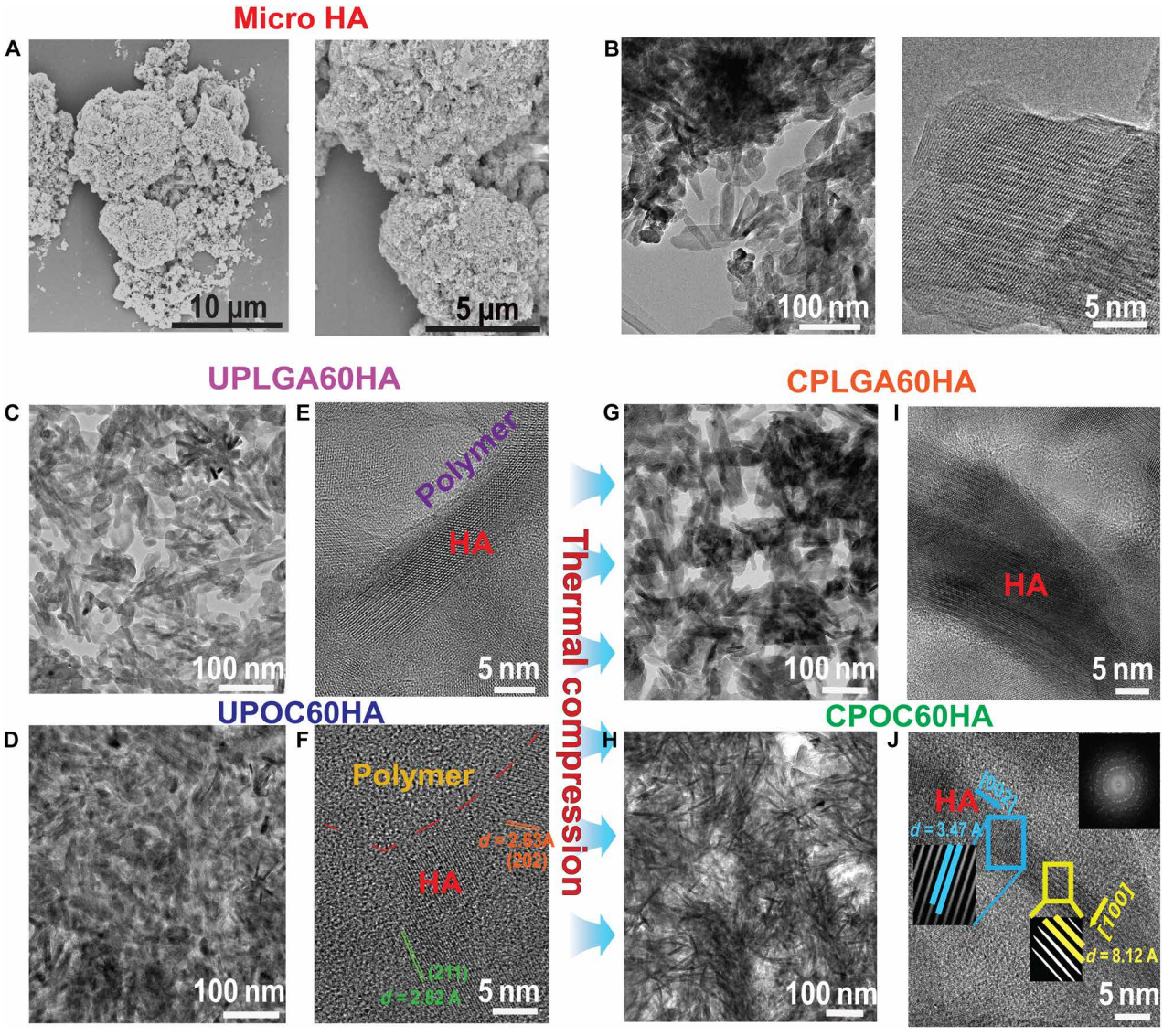

Fig. 2. Hot pressing facilitated citrification on directional recrystallization of HA. (**A**) Scanning electron microscopy images of HA microparticles. Larger magnification shown on the right. (**B**) STEM images of HA reference powder in nanoscale. (**C**) Representative STEM images of UPLGA60HA and its larger magnification on the right (**E**). (**D**) Representative STEM images of UPOC60HA and its larger magnification on the right (**F**). (**G**) Representative STEM images of CPLGA60HA and its larger magnification on the right (**I**). (**H**) Representative STEM images of CPOC60HA and its larger magnification on the right (**J**). The yellow box in (J) using FFT and inverse FFT to locate (100) plane and [100] direction which represent the width of the HA fiber; blue box indicates the (002) plane and [002] direction of HA fibers which represent the length.

to D). Upon hot pressing, ion-facilitated recrystallization in CPOC60HA adjusted the Ca/P ratio to ~1.84, approximating that of natural bone, whereas CPLGA60HA failed to establish such a biomimetic environment, highlighting POC's distinctive capacity to modulate HA integration and composition.

To validate the integration of HA with POC after hot pressing, we conducted x-ray photoelectron spectroscopy (XPS) and solid-state nuclear magnetic resonance (ssNMR). XPS confirmed the formation of ionic bonds between HA and POC oligomer in UPOC60HA, as evidenced by the shift in Ca 2p3/2 from 346.5 to 346.9 eV, reflecting higher binding energy between Ca and carboxylates (Fig. 4D). Notably, this binding energy remained unchanged postrecrystallization, indicating the persistence of ionic networks within the crosslinked POC-HA matrix. The Ca environment in CPOC60HA closely matched that of sheep femur, where citrate facilitates apatite and collagen integration, suggesting strong biomimicry, confirmed by XPS spectra of citrate-treated HA (fig. S5, A to E). Further XPS analysis of C 1s, P 2p, and O 1s spectra revealed changes in the phosphate environment due to POC incorporation post–hot pressing (fig. S5, F to I).

To further validate the organic interfusion on inorganic mineral and characterize its thermal behavior, differential scanning calorimetry (DSC) was conducted on HA, CPOC60HA, and sheep femur. The DSC profiles of CPOC60HA and sheep femur were overlapping to each other below 400°C, highlighting the similarity of their organic decomposition, which was not observed in HA alone (Fig. 4E and fig. S6, A to C). The appearance of the endothermic and endothermic transition peak at ~740°C in CPOC60HA, absent in HA, indicates that POC modified the crystalline structures of HA. At higher

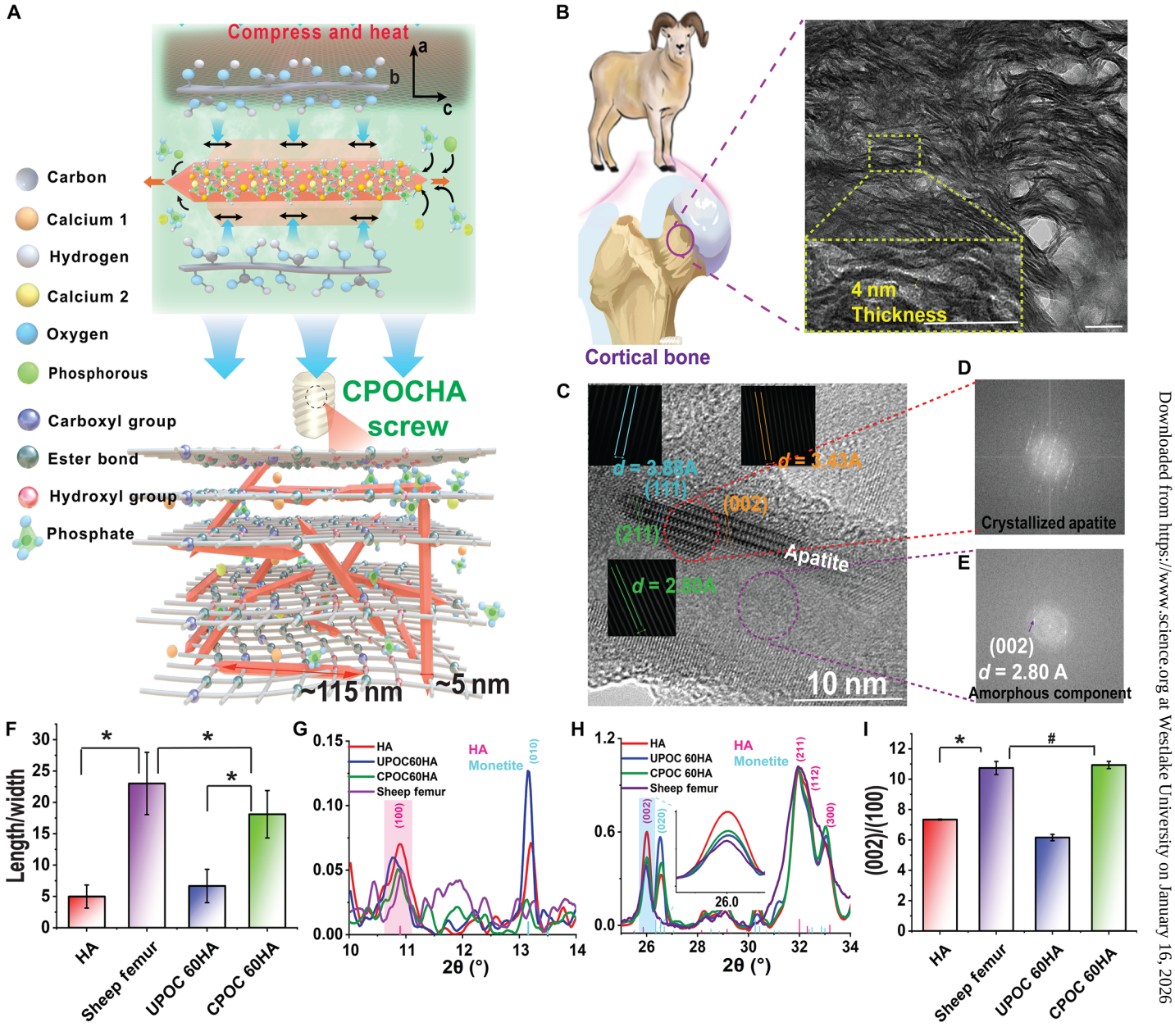

Fig. 3. Hot pressing induced apatite nanorods that closely resemble those found in sheep cortical bone. (**A**) Scheme for construction of FDA-approved bone screw using UPOC60HA. Ion-rich bath in UPOC60HA facilitated recrystallization. The fibers generated under hot pressure and polymeric limitation were highlighted. HA rod shown in Fig. 1 underwent citrification into slim and elongated nanorods, homogeneously distributed within cross-linked polymeric networks. (**B**) A cross-sectional image of cortical bones that contain multiple thin and fine fibers. Scale bar, 50 nm. (**C** to **E**) At the nanoscale, it composed of well-ordered (D) and disordered (E) phases with their corresponding FFT spectra. The ordered phase (C) showing arrangement of apatite and corresponding of inverse FFT pattern illustrating (002), (111), and (211) reflections representing the HA nanocrystals. (**F**) Summarized ratio of length to width of HA from each specimen. XRD spectra of species focusing on (**G**) (100) and (**H**) (002) plane of HA exhibited the recrystallization under POC treatment and hot pressing, showing the highly biomimicry properties to apatite found in sheep bone. (**I**) Ratios between peak intensity of (002) and (100) each specimen summarized from XRD spectra. Data point in (F) and (I) represents average, $n = 10$ and $n = 3$, respectively, while error bars represent SD. * represents the statistical significance ($P < 0.05$), and # represents the nonstatistical significance ($P > 0.05$).

temperatures, HA microparticles displayed two pronounced endothermic events at 955° and 1234°C, associated with dehydroxylation and structural rearrangement of crystalline (*49*, *50*). In contrast, these endothermal peaks shifted to 1091° and 1343°C in CPOC60HA, and similar peak profiles were also observed in sheep femur, indicating biomimcry and enhanced thermal stability (fig. S6D). Collectively, these results demonstrate that POC effectively modified HA microparticles and that the recrystallized HA formed under POC influence exhibits thermal behaviors similar to natural bones at higher temperatures. This behavior confirms strong citrate-mediated interaction with HA and supports the role of POC in transforming the as-used HA microparticles into a biomimetic mineral phase, resembling

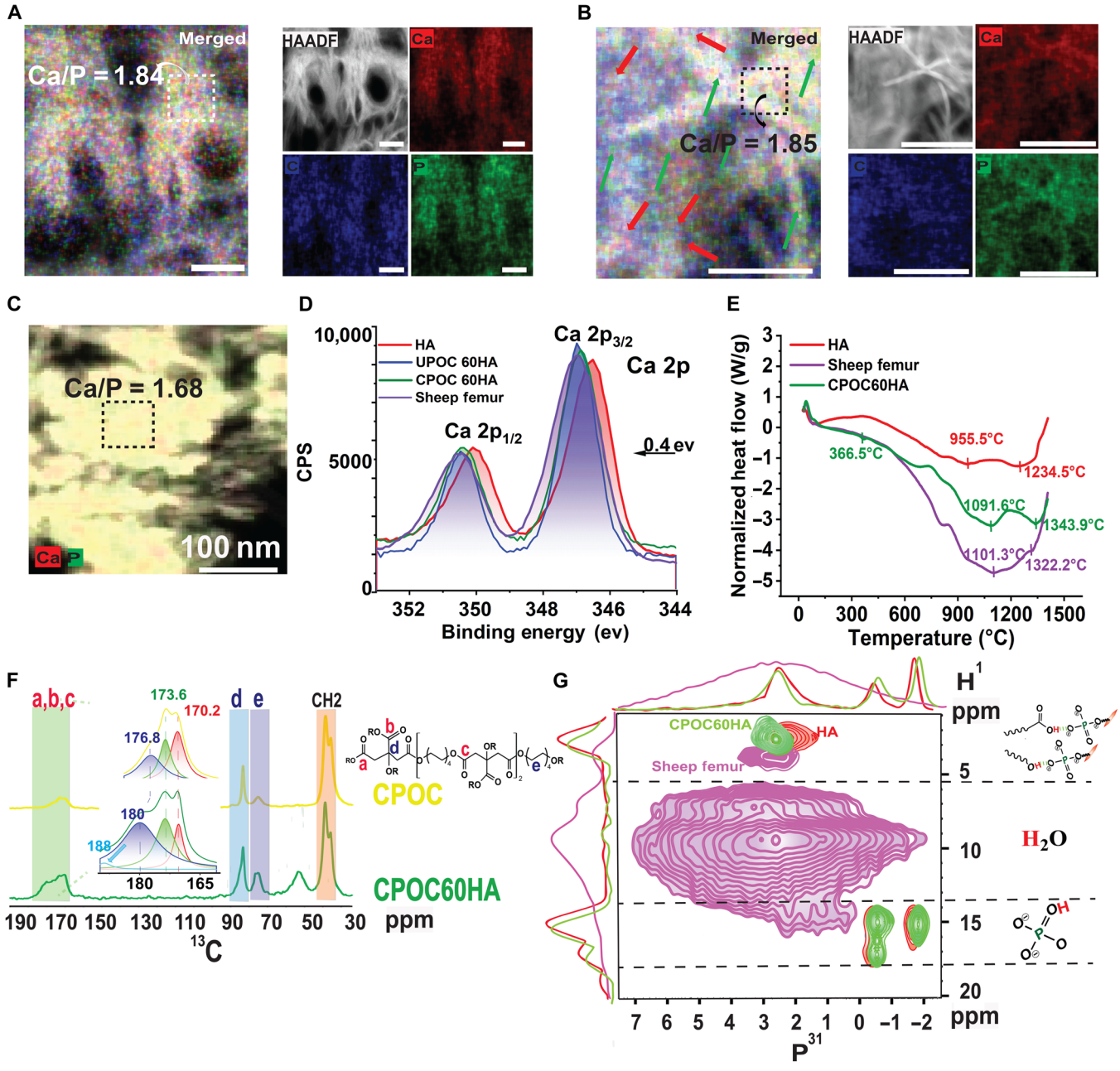

Fig. 4. Characterization of recrystallized HA within POC matrix. (**A**) EDS images of sheep femur cortical bone. Scale bars, 60 μm. (**B**) EDS images of HA nanorods in CPOC60HA which exhibited high similarity of element distributions by showing distinct Ca (red) and P (green) within polymeric matrix. Scale bars, 40 μm. (**C**) EDS mapping at nanoscale of HA powder. (**D**) High-resolution of XPS survey spectra of HA, UPOC60HA, CPOC60HA, and sheep femur, focusing on Ca 2p in binding energy range of 353 to 344 eV and a doublet $2p_{1/2}$ and $2p_{3/2}$ because spin-orbital splitting was observed. (**E**) DSC profiles of HA microparticles, sheep femur, and CPOC60HA from 25° to 1400°C. (**F**) The ^{13}C cross-polarization spectrum of POC and CPOC60HA, and the carbon near reactive sites is labeled as discussed in the text. (**G**) 2D $^{1}H - {}^{31}P$ HetCor experiments recorded on HA (red), CPOC60HA (green), and natural sheep femur (purple) [contact time (CT) = 500 μs] reveal the reactive sites near different phosphate in each specimen. HAADF, high-angle annular dark field. CPS, counts per second.

that in sheep femur. To identify specific POC binding sites on HA, ^{13}C cross-polarization NMR spectroscopy revealed a shoulder peak at 73.8 parts per million (ppm), corresponding to quaternary carbon near unreacted carboxyl and hydroxyl groups. Ester bond formation was confirmed at 170.2 and 173.6 ppm. The downshift of unreacted carboxyl groups from 176.8 to 180 ppm indicated interactions with electron-withdrawing phosphate, while a shoulder peak at 188 ppm was attributed to citrate-derived carboxylates (Fig. 4E and fig. S7A).

We also analyzed the pair distribution function (PDF) from XRD data, focusing on the Ca—O coordination environment in an atomic level. The peak at ~2.5 Å reflected the coordination number of Ca—O bonds (*51*). The increase in integration suggested cross-linking of

POC and HA through inorganic ionic bonds in UPOC60HA. Hot pressing further increased the Ca—O coordination number in CPOC60HA (fig. S8, A and B), and the similar increased binding between organic and inorganic phases was also observed in citrate-treated HA (fig. S8, C and D). Carbonyl changes in FTIR spectra further validated the strengthening of crosslinking upon thermal pressing (fig. S8E).

Two-dimensional ^{1}H-^{31}P heteronuclear correlation (Hetcor) ssNMR which revealed the correlation between ^{1}H signals and phosphorous in apatite was conducted to further confirm the interactions between POC and HA. In the HA reference, the ^{1}H signal centered at 2.7 ppm, while its corresponding ^{31}P centered at 2.3 ppm, indicating hydroxyl groups associated with phosphate (*52*, *53*). After recrystallization, the ^{31}P peak in CPOC60HA shifted moderately to 2.5 ppm, while the ^{1}H remained constant. This suggested additional interactions between phosphate and hydroxyl originating from POC rather than the intrinsic HA reference, further validating the presence of ionic bonding between cross-linked POC and recrystallized HA (Fig. 4F and fig. S9, A and B).

In contrast, CPLGA60HA did not exhibit notable shifts compared to HA reference, indicating weaker interactions between PLGA and HA (fig. S10). Notably, the linkages between PLGA and HA were disrupted by hot press–induced recrystallization, leading to marked phase separation and underscoring POC's superior chelating ability, which preserved interfacial linkages and sustained integration of HA crystallites during recrystallization. On the basis of our findings, we conclude that achieving biomimetic nanorods and a homogeneous organic-inorganic hybrid requires dual reactivity between both components. POC demonstrated greater specificity and reactivity toward HA than PLGA, enabling formation of nanostructures with chemical and physical properties closely resembling natural bone. These results highlight the robust ionic interactions between cross-linked POC and HA and reinforce the POC's unique role in promoting directional HA recrystallization with excellent physical and biomimetic properties.

Crystallinity and hydration as determining factors in initiation of citrification

Beyond investigating the biomimetic modulation conferred by the citrate-based polymer, we sought to elucidate the critical role of the inorganic component. Specifically, we demonstrate that HA microparticles must have properties, namely, susceptibility to citrate-induced dehydroxylation and ion release that enable their facile transformation into biomimetic nanorods. This dual organic-inorganic strategy established an optimal interface and drove the concurrent dissolution-recrystallization reactions essential for superior composite integration. To this end, we fabricated POC60HA composites using highly crystallized (HC) HA with elevated hydroxylation levels but similar particle sizes (fig. S11, A to D). However, the carbonyl shoulder peak was not observed in the FTIR spectrum of uncross-linked POC60HA using HC HA (HUPOC60HA), nor was it observed in the thermally compressed composites (HCPOC60HA) (Fig. 5A). The addition of POC only slightly reduced hydroxylation and increased Ca/P ratios, and thermal treatment restored hydroxylation and crystallinity to their original levels (tables S3 and S4).

Similar phenomena were observed in high-resolution XPS spectra of Ca and P environments that treatment of POC oligomer triggered the high energy shifting in Ca 2*p* and P 2*p*, but the recrystallization of HC HA restored the chemical environment back to original states (Fig. 5, B and C), indicating the breakage between HC HA and cross-linked POC and failure of creating HA nanorods (fig. S11E). PDF analysis and C1s spectra also exhibited the opposite trend as we observed in CPOC60HA, which illustrated the weak installation of cross-linked POC with HC HA, therefore phase separation (fig. S11, F and G). Although smaller HA crystals formed in HCPOC60HA after the hot pressing of HUPOC60HA, nanorod structures were not observed in either the TEM or EDS images. Moreover, distinct boundaries between the HA particles and the polymer matrix remained clearly visible, demonstrating poor interfusion between HC HA and POC, resulting in poor mechanical properties in comparison to that of CPOC60HA (Fig. 5, D to F, and figs. S11H and S12A). In summary, these results highlighted the necessity of dehydroxylation of HA as the onset of citrification to expose enough binding sites for POC to create a nourished environment for nanorod recrystallization.

Collectively, this study uncovers a mechanism by which a soft and elastic citrate-based polymer, POC, citrates HA to form super-strong, bone-mimicking POC/HA nanocomposites. In this top-down approach, POC induces partial dissolution of HA microparticles, generating an ion-rich environment that blurs organic-inorganic boundaries and facilitates the formation of ultrathin HA nanorods under hot pressing, closely mimicking the hierarchical architecture of natural bone with HA content up to 60 wt %. Thereof, hot pressing further drives directional HA recrystallization, converting microparticles into nanorods that preferentially elongate along the *c* axis while limiting lateral growth. In contrast to conventional PLGA, which offers only modest strength gains, the POC-enabled citrification process emulates citrate's natural role, yielding composites with compressive strengths exceeding 250 MPa. These findings reveal the critical function of citrate-based polymers and hot pressing in creating biomimetic orthopedic nanocomposites and establish a molecular engineering strategy for next-generation load-bearing implants and beyond.

DISCUSSION

Our findings redefine the structure-property paradigm for polymer-mineral composites by demonstrating that soft and elastic polymers can achieve superior strength when coupled with hierarchical mineral transformation. Conventional strategies typically rely on rigid polymers, such as PLGA or PMMA, to enhance stiffness; however, these materials provide limited mechanical improvement (usually below 50 MPa) and often suffer from poor toughness due to weak organic-inorganic interfaces. In contrast, POC, despite its intrinsic softness, actively mediates HA dehydroxylation and ion release, establishing a dynamic organic-inorganic interface that drives directional recrystallization. Under hot pressing, this top-down citrification process yields ultrathin (~5 nm) HA nanorods with preferential *c*-axis elongation and suppressed lateral growth, closely resembling the apatite morphology found in natural bone. The resulting composites exhibit blurred organic-inorganic boundaries and restored bone-like Ca/P ratios (~1.84) and compressive strengths exceeding 250 MPa, surpassing conventional polymer-HA systems.

A critical factor in this process is the crystallinity of the starting mineral. Highly crystalline HA resists citrate-induced modification and fails to transform into nanorods, indicating that a labile, poorly crystalline phase is essential for initiating citrification and enabling hierarchical integration. This mirrors bone biology, where immature, low-crystallinity apatite enables remodeling and integration within collagen fibrils. In the context of POCHA composites, low-crystallinity and partially dehydroxylated HA facilitates strong interfacial bonding with POC, enabling directional recrystallization and resulting in

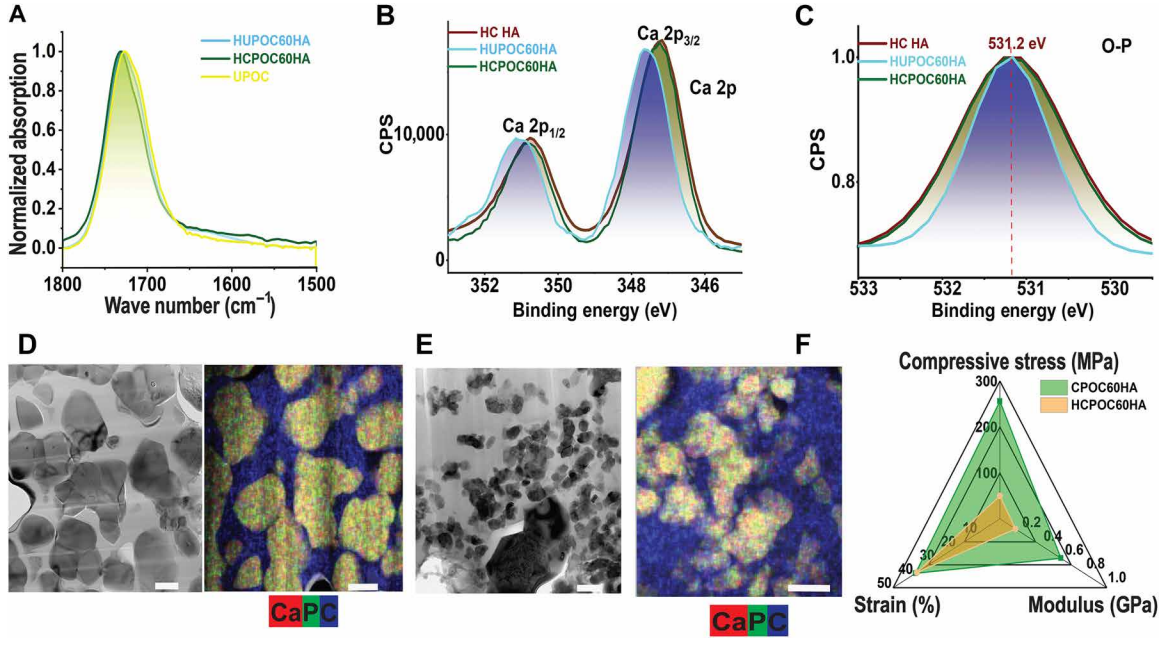

Fig. 5. Necessity of citrification on HA particles. (**A**) FTIR spectra of UPOC, HUPOC60HA, and HCPOC60HA, focusing on carbonyl groups. (**B**) High-resolution XPS spectra of HC HA, HUPOC60HA, and HCPOC60HA, focusing on Ca 2p peaks in binding energy range of 353 to 345 eV. (**C**) Detailed spectra of O-P of all three specimens show that the chemical states of O-P were not affected by addition of HA and hot pressure. (**D**) TEM and EDS images of HUPOC60HA. Scar bars, 200 nm. (**E**) TEM and EDS images of HCPOC60HA with failure of generation of nanorods. (**F**) Comparison of mechanics between CPOC60HA and HCPOC60HA, highlighting the importance of creating well-integrated organic HA.

high load-bearing performance. These interactions promote localized release of calcium and phosphate ions, creating an ion-rich microenvironment that drives the transformation of HA microparticles into nanorods during recrystallization. This work underscores the critical role of mineral crystallinity and hydroxylation state in achieving well-integrated organic-inorganic composites and provides valuable insight for designing next-generation high load-bearing biomimetic materials.

Despite successfully replicating *c*-axis–oriented apatite nanorods, the lateral packing in POCHA remains less ordered than that guided by collagen in natural bone. While POC is effective in directing longitudinal mineral growth and establishing a bone-like chemical environment, it may be insufficient on its own to regulate higher-order lateral organization. However, in our knowledge, the ability of POC to generate aligned apatite nanorods and organic-inorganic integration that closely mimic those of nature bones still represents a substantial advancement in biomimetic orthopedic composite design.

Although citrate plays a central role in mediating HA transformation in this study, other polymers containing multiple carboxyl groups may also interact with HA. For example, previous work has shown that pectin, rich in carboxyl functionalities, can induce the formation of smaller HA crystals and even nanoscale fibrous morphologies (*46*), supporting the general concept that multidentate carboxyl-containing molecules can regulate apatite nucleation and crystal growth. However, these systems operate primarily in ionic solution environments and promote in situ mineral nucleation. In contrast, our work uses a top-down strategy, transforming HA microparticles within a polymeric matrix. Furthermore, in those advanced polymer-induced liquid precursor systems, the thickness of synthesized HA platelets typically ranges from ~12 to 20 nm. By comparison, the HA nanorods in POCHA composites achieve ultrathin dimensions of ~5 nm, which are much closer to those found in natural bone. This distinction highlights that, while other carboxyl-rich polymers can modulate HA nucleation, citrate-based polymer (POC) uniquely enables both chemical modification and morphological transformation of HA microparticles for engineering highly biomimetic nanostructures.

Beyond structural and mechanical improvements, the strong ionic bonding between POC and HA may enhance biological performance by promoting osteoblast adhesion and facilitating matrix mineralization. Citrate-based polymers like POC are already FDA approved for orthopedic applications, underscoring their clinical relevance. The ionic exchange inherent to this recrystallization process further enables tunability of both mechanical and biological properties. Looking ahead, ionic substitutions, such as partial replacement of Ca^{2+} with Sr^{2+}, could stabilize the apatite lattice, enhance osteogenesis, and inhibit osteoclastic resorption, thereby adding therapeutic functionality (*54*, *55*).

The goal of this study is to establish a mechanism-based framework of using a unique citrate-mediated citrification and hot pressing process to replicate the key features of natural bone. Biomimetic materials are highly valued because they can reduce immune rejection, improve host integration, and enhance regenerative outcomes. The closer the synthetic material resembles native tissue in chemistry, structure, and function, the more effectively it can support successful tissue repair. This work demonstrates that by understanding and recapitulating fundamental biological mechanisms, such as citrate-regulated mineral transformation and *c*-axis oriented apatite growth, it is possible to engineer composites with both bone-like nanostructure and mechanical competence. Rather than simply adding inorganic fillers to polymers or unanimously adopting strong and stiff polymers for compositing with inorganic minerals, we show that the quality of

organic-inorganic integration between soft and elastic polymers and inorganic minerals, driven by molecular-level interactions, is a key determinant of load-bearing capacity of the composite material. We believe that this study shifts the orthopedic biomaterials field toward a more mechanism-driven approach for biomimicry, where materials are not only inspired by nature but also reproduce its functional principles. This paradigm provides a strong foundation for the development of next-generation, clinically relevant biomaterials, especially orthopedic materials for bone repair and regeneration.

Collectively, this work shifts the composite design paradigm away from "stronger polymers for stronger composites" toward a biomimetic soft materials—mineral synergy that mirrors collagen—apatite interactions in bone. POC-enabled citrification offers a scalable molecular strategy for engineering biodegradable orthopedic implants that combine mechanical robustness, bone-like nanostructure, and biological functionality.

MATERIALS AND METHODS

POC/PLGA-HA composite preparation

Materials

Hydroxyapatite (HA) {molecular weight: 502.32, assay > 90% [as $Ca_5(PO_4)_3OH$]; particle size > 75 μm [0.5%], 45 to 75 μm [1.4%], <45 μm [98.1%]} was purchased from Sigma-Aldrich (St. Louis, MO, USA) (*56*, *57*). Ingredients of polymer synthesis:citric acid (CA) and 1,8-octandiol were also purchased from Sigma-Aldrich (St. Louis, MO, USA). Poly(D,L-lactide-*co*-glycolide) (75:25 lactide:glycolide, acid end-capped, Mn: 55,000 to 65,000 Da) (PLGA) was purchased from PolySciTech (West Lafayette, IN, USA).

POC prepolymer synthesis

POC prepolymers were synthesized by the copolymerization of CA and 1,8-octandial in a 1:1 molar ratio. The mixture of CA and 1,8-octandial were added into a round-bottom flask and melted under a flow of nitrogen gas by stirring at 160°C in oil bath for 10 min. Then, the temperature was lowered to 140°C, and the reaction was proceeded for 2 hours to make POC prepolymer. 1,4-Dioxane was added into the flask to stop the reaction when the stirring speed reached 60 rpm. To purify the POC prepolymer, the prepolymer dissolved in 1,4-dioxane was precipitated in deionized (DI) water produced from a Direct-Q5 Water Purification System (Milipore, Billerica, MA). The white precipitates were lyophilized in a Freezone 6 Freeze Dryer (Labconco, Kansas City, MO) to make purified POC prepolymer ready for composite synthesis (*33*).

Synthesis of POC-HA composites

POC prepolymer was dissolved in 1,4-dioxane to make 60 wt % solution. Then, HA powder was added to the solution in various weight ratios. The composites were put under air flow to evaporate the solvent for 3 days. The resulting composites were denoted as uncrosslinked POC-X HA composites where X represents the HA weight percentage in the composites. Uncrosslinked composites were inserted into metal mold under compression (200 kg/cm^2) for 1 day followed by putting whole mold into oven with 80°C for 3 days and 120°C for another 3 days to make compressed POC-X HA composites (fig. S1) (*34*).

Synthesis of PLGA-HA composites

PLGA was dissolved in 1,4-dioxane to make 60 wt % solution. Then, the procedures of making uncrosslinked (denoted as untreated in PLGA composites) and compressed composites are the same as we performed in POC-XHA composites.

CA-treated HA fabrication: The fabrication followed the reported procedure. A solution of CA (10/200/500 μM/1 M) in DI water (50 ml) was maintained at 37°C, and the pH was adjusted to 5.52 by dropwise addition of concentrated NaOH solution. HA powder (800 mg) was then added, and the pH of the resulting suspension was adjusted to 6.5 by dropwise of concentrated NaOH. The suspension was stirred and set at room temperature for 7 days. Then, the solid was washed by DI water and dried in air, which was ready for subsequent characterizations.

Composite mechanics

Cylinder compression tests were performed using a 5966 series advanced electromechanical testing system with a 10kN load cell (Instron, Norwood, MA, USA). Cylinder shaped samples 6.5 mm by 13 mm (diameter by height) were compressed at a rate of 1.3 mm min^{-1} until there was 10% loss on compression stress. Values were converted to stress (megapascals), and initial modulus (megapascals) was calculated from the first 10% compression strain.

Composite structural characterizations

ATR-FTIR characterization was performed on a Bruker Vertex 70 FTIR spectrometer with a Pike Miracle Single-Bounce diamond crystal plate accessory at room temperature. The spectra were recorded over a wavelength between 4000 and 500 cm^{-1} with a resolution of 6 cm^{-1}. For analysis of raw spectra, the carbonyl groups of polymers were baselined from 1800 to 1700 cm^{-1}. For inorganic minerals, V_1 and V_3 PO_4 ranged from 1200 to 900 cm^{-1}, and V_4 PO_4 are from 700 to 500 cm^{-1}. The acidic phosphate is assigned between 900 and 800 cm^{-1}. The splitting factor (SF) was calculated as the sum of the intensity of 560 and 600 cm^{-1} divided by the intensity of the hollow between two peaks, which was illustrated below (*58*)

$$\mathrm{Xc\ (SF)} = \frac{\left(I_{560} + I_{600}\right)}{I_{\mathrm{hollow}}} \quad (1)$$

To obtain more detailed information from ATR-FTIR spectra, the raw spectra between 1150 and 500 cm^{-1} were processed using Lorentzian curve fitting (R^2 above 0.99) to achieve fitness in all samples in the data analysis and graphing software OriginPro 2021 (OriginLab). Several peaks in V_1 and V_3 PO_4 regions were fitted and analyzed, including peaks at ~1110, 1090, 1055, 1020, 999, and 960 cm^{-1}. Peak area percentages, heights, and width of these specific peaks were determined.

Composites mineral morphology and characterization

X-ray diffraction

HA powders were analyzed using a Malvern Panalytical Empyrean III (Malvern, UK) with silicon zero-background flat stage accessory. Other uncrosslinked, uncompressed, and compressed composites were analyzed using programmable Z stage with manual phi, and dial gauge was used to adjust the height before measurements. The patterns were collected with 0.02° 2θ step size from 5° to 70°and 99 s per step with 0.06°/s scan speed. The spectra were fitted with a Lorentzian curve ($R^2 > 0.99$) using OriginPro software (OriginLab) to determine the peak area and FWHM to measure the crystallinity (Xc), microstrain (ε), and crystal size (D) based on the illustrated equations below (*59*, *60*)

$$\mathrm{Xc} = 1 - V\frac{112}{300} / I_{300} \quad (2)$$

where V represents the intensity of hollow between (112) and (300) plane peaks.

$$\varepsilon = \frac{\mathrm{FWHM}}{4\tan\theta} \quad (3)$$

where FWHM is in radians.

$$D = \frac{K\lambda}{\mathrm{FWHM}\ \cos\theta} \quad (4)$$

where K represents the crystal shape factor (0.9 for bone apatite), λ is the x-ray wavelength (1.54 Å for Cu K_α), and FWHM is in radians.

Because of the observation of monetite in commercial HA powder, we calculated the percentage of HA and monetite within the powder by dividing the peak area of HA to all peaks.

The PDF was calculated from the diffraction data using PDFgetX3 software (*61*) (version 2.2.1). All parameters were applied according to the instructions. Then, integration (I) of peak at ~2.5 Å was calculated with the following equations

$$I = 4\pi\rho \int_{r\min}^{r\max} sg(r)r2\mathrm{d}r$$

where the peak at ~2.5 Å is located between $r_{\min}$ and $r_{\max}$, which is contributed by the coordination between Ca and O. ρ is the number density for HA. Integration (I) reflected the tendency of Ca—O coordination when integrating with POC after thermal compression.

Scanning electron microscopy

The morphology and particle size of HA powders were characterized using a Thermo Fisher Scientific Apreo scanning electron microscope. Samples were suspended in acetone, and the droplet was gently spread onto carbon tape adhered to aluminum stubs and sputter-coated with a thin layer of iridium to minimize charging. Imaging was performed under high vacuum conditions at an accelerating voltage of 5 kV and a beam current of 50 pA.

Scanning transmission electron microscopy

The microstructures of the samples were observed using an FEI Titan3 G2 double aberration-corrected microscope at 300 kV. EDS elemental maps of the sample were collected by using a SuperX EDS system under STEM mode. All STEM images were collected by using a high-angle annular dark-field detector which had a collection angle of 52 to 253 mrad.

Thin cross-sectional transmission electron microscopy (TEM) specimens of the bulk samples were prepared by using a focused ion beam (FIB; FEI Helios 660) lift-out technique. A thick protective amorphous carbon layer was deposited over the region of interest, and then Ga^+ ions (30 kV and then stepped down to 1 kV to avoid ion beam damage to the sample surface) were used in the FIB to make the samples electron transparent. The original powder samples were prepared by using the standard drop-casting method on lacey carbon TEM grids.

X-ray photoelectron spectroscopy

XPS experiments were performed using a Physical Electronics VersaProbe III instrument equipped with a monochromatic Al kα x-ray source ($h\nu$ = 1486.6 eV) and a concentric hemispherical analyzer. Charge neutralization was performed using both low energy electrons (<5 eV) and argon ions. The binding energy axis was calibrated using sputter-cleaned Cu (Cu $2p_{3/2}$ = 932.62 eV, Cu $3p_{3/2}$ = 75.1 eV) and Au foils (Au $4f_{7/2}$ = 83.96 eV). Peaks were charge referenced to CH_x band in the carbon 1s spectra at 284.8 eV. Measurements were made at a takeoff angle of 45° with respect to the sample surface plane. This resulted in a typical sampling depth of 3 to 6 nm (95% of the signal originated from this depth or shallower). Quantification was done using instrumental relative sensitivity factors that account for the x-ray cross section and inelastic mean free path of the electrons. On homogeneous samples, major elements (>5 atom%) tend to have SDs of <3%, while minor elements can be significantly higher. The analysis size was ~200 μm in diameter.

Sample preparation for ssNMR

Each sample was milled into fine particles in a Retsch CryoMill consisting of two stainless steel vessels. The mill was equipped with enclosed liquid nitrogen (LN_2) autofill system. The 50-ml chromium stainless steel chamber filled with a 5-g sample equipped with a 25-mm grinding ball was prepared for cryomilling process. Precooling on each sample in LN_2 was carried out for 10 min. Then, the mill was operated to shake with 5 cycles where 1 cycle included 2 min of shaking at 25 Hz and 1 min of rest. After the cryomilling, the powder of each sample was collected and stored in 4°C for further ssNMR measurements.

Solid-state nuclear magnetic resonance

^{1}H, ^{31}P, and ^{13}C solid-state magic angle spinning NMR experiments were carried out on a Bruker Avance III HD 500 MHz spectrometer using a 4-mm triple resonance cross-polarization magic angle spinning (CPMAS) probe. All measurements were performed with a magic spinning frequency of 12 kHz. All 1D ^{31}P CPMAS spectra were acquired with 64 scans with contact time (CT) = 4 ms and relaxation delay (RD) = 5 s. 2D -^{1}H^{31}P HetCor spectra were recorded with eight scans per evolution increment with a total of 64 increments with frequency-switched Lee-Goldburg proton decoupling with RD = 5 s and CT = 500 μs. ^{13}C CPMAS spectra were recorded with 8192 scans with RD = 5 s and CT = 2 ms for all composites and polymers. For CA and CA-treated HA samples, CT was adjusted to 3 ms. For ^{1}H NMR spectra, because of limited spinning frequency, the spectra were not highly resolved but could still provide useful data to explain the chemical structure of composites. ^{1}H NMR spectra were collected with a short 1-μs single pulse excitation with 16 scans and 5-s recycle delay.

Differential scanning calorimetry

Data were collected using a simultaneous thermal analyzer (SDT650) from TA Instruments Inc. (Delaware, USA). The samples (~12 mg) were transferred into the analyzer, and the measurements were performed from room temperature to 1400°C under ultrahigh purity of nitrogen with a heating rate of 5°C/min. A 15-min purge time was used to ensure that samples were under inert atmosphere before heating initiated.

Statistical analysis

One-way analysis of variance (ANOVA) was performed on three or more means with a t test applied within groups. A $P < 0.05$ was considered to be significant.

Supplementary Materials

This PDF file includes:

Tables S1 to S4
Figs. S1 to S12
References

REFERENCES

1. B. Yuan, L. Wang, R. Zhao, X. Yang, X. Yang, X. Zhu, L. Liu, K. Zhang, Y. Song, X. Zhang, A biomimetically hierarchical polyetherketoneketone scaffold for osteoporotic bone repair. *Sci. Adv.* **6**, eabc4704 (2020).
2. S. J. Hollister, Porous scaffold design for tissue engineering. *Nat. Mater.* **4**, 518–524 (2005).

3. B. Zhang, J. D. Skelly, J. R. Maalouf, D. C. Ayers, J. Song, Multifunctional scaffolds for facile implantation, spontaneous fixation, and accelerated long bone regeneration in rodents. *Sci. Transl. Med.* **11**, eaau7411 (2019).
4. J. Wei, Y. Yan, J. Gao, Y. Li, R. Wang, J. Wang, Q. Zou, Y. Zuo, M. Zhu, J. Li, 3D-printed hydroxyapatite microspheres reinforced PLGA scaffolds for bone regeneration. *Biomater. Adv.* **133**, 112618 (2022).
5. X. Song, W. Guan, H. Qin, X. Han, L. Wu, Y. Ye, Properties of poly(lactic acid)/walnut shell/hydroxyapatite composites prepared with fused deposition modeling. *Sci. Rep.* **12**, 11563 (2022).
6. I. S. Komang-Agung, L. Hydravianto, O. Sindrawati, P. William, Effect of polymethylmethacrylate-hydroxyapatite composites on callus formation and compressive strength in goat vertebral body. *Malays. Orthop. J.* **12**, 6–13 (2018).
7. G. He, T. Dahl, A. Veis, A. George, Nucleation of apatite crystals in vitro by self-assembled dentin matrix protein 1. *Nat. Mater.* **2**, 552–558 (2003).
8. Y. Wang, T. Azaïs, M. Robin, A. Vallée, C. Catania, P. Legriel, G. Pehau-Arnaudet, F. Babonneau, M.-M. Giraud-Guille, N. Nassif, The predominant role of collagen in the nucleation, growth, structure and orientation of bone apatite. *Nat. Mater.* **11**, 724–733 (2012).
9. E. Davies, K. H. Muller, W. C. Wong, C. J. Pickard, D. G. Reid, J. N. Skepper, M. J. Duer, Citrate bridges between mineral platelets in bone. *Proc. Natl. Acad. Sci. U.S.A.* **111**, E1354–E1363 (2014).
10. C. Shao, R. Zhao, S. Jiang, S. Yao, Z. Wu, B. Jin, Y. Yang, H. Pan, R. Tang, Citrate improves collagen mineralization via interface wetting: A physicochemical understanding of biomineralization control. *Adv. Mater.* **30**, 1704876 (2018).
11. X. Li, Q. Zou, H. Chen, W. Li, In vivo changes of nanoapatite crystals during bone reconstruction and the differences with native bone apatite. *Sci. Adv.* **5**, eaay6484 (2019).
12. S. Araya, S. Saito, S. Nakanishi, Y. Kawanishi, Soluble collagen in bone. *Nature* **192**, 758–759 (1961).
13. F. Nudelman, K. Pieterse, A. George, P. H. H. Bomans, H. Friedrich, L. J. Brylka, P. A. J. Hilbers, G. de With, N. A. J. M. Sommerdijk, The role of collagen in bone apatite formation in the presence of hydroxyapatite nucleation inhibitors. *Nat. Mater.* **9**, 1004–1009 (2010).
14. T. Bian, K. Zhao, Q. Meng, Y. Tang, H. Jiao, J. Luo, The construction and performance of multi-level hierarchical hydroxyapatite (HA)/collagen composite implant based on biomimetic bone Haversian motif. *Mater. Des.* **162**, 60–69 (2019).
15. L. Yu, M. Wei, Biomineralization of collagen-based materials for hard tissue repair. *Int. J. Mol. Sci.* **22**, 944 (2021).
16. V. K. Kis, H. P. Schwarcz, N. Nassif, Z. Szekanecz, Bone mineral platelets are mesocrystals formed by monoclinic nanocrystals. *Commun. Mater.* **6**, 192 (2025).
17. H. Gao, B. Ji, I. L. Jäger, E. Arzt, P. Fratzl, Materials become insensitive to flaws at nanoscale: Lessons from nature. *Proc. Natl. Acad. Sci. U.S.A.* **100**, 5597–5600 (2003).
18. Y. Y. Hu, A. Rawal, K. Schmidt-Rohr, Strongly bound citrate stabilizes the apatite nanocrystals in bone. *Proc. Natl. Acad. Sci. U.S.A.* **107**, 22425–22429 (2010).
19. A. Lotsari, A. K. Rajasekharan, M. Halvarsson, M. Andersson, Transformation of amorphous calcium phosphate to bone-like apatite. *Nat. Commun.* **9**, 4170 (2018).
20. L. Chen, Q. Yu, Y. Wang, H. Li, BisGMA/TEGDMA dental composite containing high aspect-ratio hydroxyapatite nanofibers. *Dent. Mater.* **27**, 1187–1195 (2011).
21. K. He, M. Sawczyk, C. Liu, Y. Yuan, B. Song, R. Deivanayagam, A. Nie, X. Hu, V. P. Dravid, J. Lu, C. Sukotjo, Y.-p. Lu, P. Král, T. Shokuhfar, R. Shahbazian-Yassar, Revealing nanoscale mineralization pathways of hydroxyapatite using in situ liquid cell transmission electron microscopy. *Sci. Adv.* **6**, eaaz7524 (2020).
22. P. Pàmies, Bone's bridged layers. *Nat. Mater.* **13**, 428–428 (2014).
23. M. Iafisco, G. B. Ramírez-Rodríguez, Y. Sakhno, A. Tampieri, G. Martra, J. Gómez-Morales, J. M. Delgado-López, The growth mechanism of apatite nanocrystals assisted by citrate: Relevance to bone biomineralization. *CrstEngComm* **17**, 507–511 (2015).
24. H. Xu, S. Yan, E. Gerhard, D. Xie, X. Liu, B. Zhang, D. Shi, G. A. Ameer, J. Yang, Citric acid: A nexus between cellular mechanisms and biomaterial innovations. *Adv. Mater.* **36**, e2402871 (2024).
25. X. Tan, E. Gerhard, Y. Wang, R. T. Tran, H. Xu, S. Yan, E. B. Rizk, A. D. Armstrong, Y. Zhou, J. Du, X. Bai, J. Yang, Development of biodegradable osteopromotive citrate-based bone putty. *Small* **18**, e2203003 (2022).
26. C. Ma, X. Tian, J. P. Kim, D. Xie, X. Ao, D. Shan, Q. Lin, M. R. Hudock, X. Bai, J. Yang, Citrate-based materials fuel human stem cells by metabonegenic regulation. *Proc. Natl. Acad. Sci. U.S.A.* **115**, E11741–E11750 (2018).
27. P. A. Srere, The molecular physiology of citrate. *Nature* **205**, 766–770 (1965).
28. D. Sun, Y. Chen, R. T. Tran, S. Xu, D. Xie, C. Jia, Y. Wang, Y. Guo, Z. Zhang, J. Guo, J. Yang, D. Jin, X. Bai, Citric acid-based hydroxyapatite composite scaffolds enhance calvarial regeneration. *Sci. Rep.* **4**, 6912 (2014).
29. M. F. Guly, T. N. Pechenova, L. I. Matusevich, Pathway and enzymes of conversion of citric acid into acetyl phosphate in animal tissues. *Nature* **212**, 36–37 (1966).
30. W. He, F. J. P. Miao, D. C. H. Lin, R. T. Schwandner, Z. Wang, J. Gao, J.-L. Chen, H. Tian, L. Ling, Citric acid cycle intermediates as ligands for orphan G-protein-coupled receptors. *Nature* **429**, 188–193 (2004).
31. M. G. V. Heiden, L. C. Cantley, C. B. Thompson, Understanding the Warburg effect: The metabolic requirements of cell proliferation. *Science* **324**, 1029–1033 (2009).
32. V. Sokolova, K. Kostka, K. Shalumon, O. Prymak, J.-P. Chen, M. Epple, Synthesis and characterization of PLGA/HAP scaffolds with DNA-functionalised calcium phosphate nanoparticles for bone tissue engineering. *J. Mater. Sci. Mater. Med.* **31**, 1–12 (2020).
33. J. Yang, A. R. Webb, S. J. Pickerill, G. Hageman, G. A. Ameer, Synthesis and evaluation of poly(diol citrate) biodegradable elastomers. *Biomaterials* **27**, 1889–1898 (2006).
34. H. Qiu, J. Yang, P. Kodali, J. Koh, G. A. Ameer, A citric acid-based hydroxyapatite composite for orthopedic implants. *Biomaterials* **27**, 5845–5854 (2006).
35. C. G. Jeong, S. J. Hollister, Mechanical, permeability, and degradation properties of 3D designed poly(1,8 octanediol-co-citrate) scaffolds for soft tissue engineering. *J. Biomed. Mater. Res. B Appl. Biomater.* **93B**, 141–149 (2010).
36. J. Kwon, H. Cho, Nanomechanical characterization of bone quality depending on tissue age via bimodal atomic force microscopy. *Nanomanuf. Metrol.* **6**, 30 (2023).
37. L.-C. Gerhardt, A. R. Boccaccini, Bioactive glass and glass-ceramic scaffolds for bone tissue engineering. *Materials* **3**, 3867–3910 (2010).
38. J. D. Pasteris, B. Wopenka, J. J. Freeman, K. Rogers, E. Valsami-Jones, J. A. van der Houwen, M. J. Silva, Lack of OH in nanocrystalline apatite as a function of degree of atomic order: Implications for bone and biomaterials. *Biomaterials* **25**, 229–238 (2004).
39. W. Querido, R. Ailavajhala, M. Padalkar, N. Pleshko, Validated approaches for quantification of bone mineral crystallinity using transmission fourier transform infrared (FT-IR), attenuated total reflection (ATR) FT-IR, and raman spectroscopy. *Appl. Spectrosc.* **72**, 1581–1593 (2018).
40. B. Wopenka, J. D. Pasteris, A mineralogical perspective on the apatite in bone. *Mater. Sci. Eng. C* **25**, 131–143 (2005).
41. M. C. Chang, J. Tanaka, FT-IR study for hydroxyapatite/collagen nanocomposite cross-linked by glutaraldehyde. *Biomaterials* **23**, 4811–4818 (2002).
42. S. J. Gadaleta, E. P. Paschalis, F. Betts, R. Mendelsohn, A. L. Boskey, Fourier transform infrared spectroscopy of the solution-mediated conversion of amorphous calcium phosphate to hydroxyapatite: New correlations between x-ray diffraction and infrared data. *Calcif. Tissue Int.* **58**, 9–16 (1996).
43. N. Kourkoumelis, X. Zhang, Z. Lin, J. Wang, Fourier transform infrared spectroscopy of bone tissue: Bone quality assessment in preclinical and clinical applications of osteoporosis and fragility fracture. *Clin. Rev. Bone Miner. Metab.* **17**, 24–39 (2019).
44. Y. Yu, B. Stevensson, M. Pujari-Palmer, H. Guo, H. Engqvist, M. Eden, The monetite structure probed by advanced solid-state NMR experimentation at fast magic-angle spinning. *Int. J. Mol. Sci.* **20**, 6356 (2019).
45. N. S. El-Hansi, H. H. Said, O. S. Desouky, M. A. Khalaf, M. S. Talaat, A. M. Sallam, XRD and ATR-FTIR techniques for integrity assessment of gamma radiation sterilized cortical bone pretreated by antioxidants. *Cell Tissue Bank.* **22**, 305–321 (2021).
46. W. Fang, H. Zhang, J. Yin, B. Yang, Y. Zhang, J. Li, F. Yao, Hydroxyapatite crystal formation in the presence of polysaccharide. *Cryst. Growth Des.* **16**, 1247–1255 (2016).
47. A. L. Boskey, A. S. Posner, Formation of hydroxyapatite at low supersaturation. *J. Phys. Chem.* **80**, 40–45 (1976).
48. O. A. Tertuliano, J. R. Greer, The nanocomposite nature of bone drives its strength and damage resistance. *Nat. Mater.* **15**, 1195–1202 (2016).
49. A. J. Ruys, M. Wei, C. C. Sorrell, M. R. Dickson, A. Brandwood, B. K. Milthorpe, Sintering effects on the strength of hydroxyapatite. *Biomaterials* **16**, 409–415 (1995).
50. S. V. Dorozhkin, Calcium orthophosphates in nature, biology and medicine. *Materials* **2**, 399–498 (2009).
51. M. I. Kay, R. Young, A. Posner, Crystal structure of hydroxyapatite. *Nature* **204**, 1050–1052 (1964).
52. Y. Wang, S. Von Euw, F. M. Fernandes, S. Cassaignon, M. Selmane, G. Laurent, G. Pehau-Arnaudet, C. Coelho, L. Bonhomme-Coury, M. M. Giraud-Guille, F. Babonneau, T. Azais, N. Nassif, Water-mediated structuring of bone apatite. *Nat. Mater.* **12**, 1144–1153 (2013).
53. G. Cho, Y. Wu, J. L. Ackerman, Detection of hydroxyl ions in bone mineral by solid-state NMR spectroscopy. *Science* **300**, 1123–1127 (2003).
54. J. T. B. Ratnayake, M. Mucalo, G. J. Dias, Substituted hydroxyapatites for bone regeneration: A review of current trends. *J. Biomed. Mater. Res. B Appl. Biomater.* **105**, 1285–1299 (2017).
55. Y. Li, C. Wen, D. Mushahary, R. Sravanthi, N. Harishankar, G. Pande, P. Hodgson, Mg–Zr–Sr alloys as biodegradable implant materials. *Acta Biomater.* **8**, 3177–3188 (2012).
56. I. R. Gibson, S. M. Best, W. Bonfield, Chemical characterization of silicon-substituted hydroxyapatite. *J. Biomed. Mater. Res.* **44**, 422–428 (1999).
57. M. Akao, H. Aoki, K. Kato, Mechanical properties of sintered hydroxyapatite for prosthetic applications. *J. Mater. Sci.* **16**, 809–812 (1981).
58. T. A. Surovell, M. C. Stiner, Standardizing infra-red measures of bone mineral crystallinity: An experimental approach. *J. Archaeol. Sci.* **28**, 633–642 (2001).
59. G. M. Poralan, J. E. Gambe, E. M. Alcantara, R. M. Vequizo, X-ray diffraction and infrared spectroscopy analyses on the crystallinity of engineered biological hydroxyapatite for medical application. *IOP Conf. Ser. Mater. Sci. Eng.* **79**, 012028 (2015).

60. K. Rogers, P. Daniels, An x-ray diffraction study of the effects of heat treatment on bone mineral microstructure. *Biomaterials* **23**, 2577–2585 (2002).
61. P. Juhas, T. Davis, C. L. Farrow, S. J. L. Billinge, PDFgetX3: A rapid and highly automatable program for processing powder diffraction data into total scattering pair distribution functions. *J. Appl. Cryst.* **46**, 560–566 (2013).
62. M. H. Hassan, A. M. Omar, E. Daskalakis, Y. Hou, B. Huang, I. Strashnov, B. D. Grieve, P. Bártolo, The potential of polyethylene terephthalate glycol as biomaterial for bone tissue engineering. *Polymers* **12**, 3045 (2020).
63. N. Kraitape, C. Thongpin, Influence of recycled polyurethane polyol on the properties of flexible polyurethane foams. *Energy Procedia* **89**, 186–197 (2016).
64. P. E. Mikael, A. R. Amini, J. Basu, M. Josefina Arellano-Jimenez, C. T. Laurencin, M. M. Sanders, C. Barry Carter, S. P. Nukavarapu, Functionalized carbon nanotube reinforced scaffolds for bone regenerative engineering: Fabrication, in vitro and in vivo evaluation. *Biomed. Mater.* **9**, 035001 (2014).
65. T. Jaeblon, Polymethylmethacrylate: Properties and contemporary uses in orthopaedics. *J. Am. Acad. Orthop. Surg.* **18**, 297–305 (2010).
66. P.-L. Lin, H.-W. Fang, T. Tseng, W.-H. Lee, Effects of hydroxyapatite dosage on mechanical and biological behaviors of polylactic acid composite materials. *Mater. Lett.* **61**, 3009–3013 (2007).
67. M. Subramaniyan, S. Karuppan, S. Helaili, I. Ahmad, Structural, mechanical, and in-vitro characterization of hydroxyapatite loaded PLA composites. *J. Mol. Struct.* **1306**, 137862 (2024).
68. F. Wang, E. B. Tankus, F. Santarella, N. Rohr, N. Sharma, S. Märtin, M. Michalscheck, M. Maintz, S. Cao, F. M. Thieringer, Fabrication and characterization of PCL/HA filament as a 3D printing material using thermal extrusion technology for bone tissue engineering. *Polymers* **14**, 669 (2022).
69. S. Eshraghi, S. Das, Micromechanical finite-element modeling and experimental characterization of the compressive mechanical properties of polycaprolactone–hydroxyapatite composite scaffolds prepared by selective laser sintering for bone tissue engineering. *Acta Biomater.* **8**, 3138–3143 (2012).
70. J. Du, Y. Zuo, L. Lin, D. Huang, L. Niu, Y. Wei, K. Wang, Q. Lin, Q. Zou, Y. Li, Effect of hydroxyapatite fillers on the mechanical properties and osteogenesis capacity of bio-based polyurethane composite scaffolds. *J. Mech. Behav. Biomed. Mater.* **88**, 150–159 (2018).
71. S. D. Mustafov, F. Sen, M. O. Seydibeyoglu, Preparation and characterization of diatomite and hydroxyapatite reinforced porous polyurethane foam biocomposites. *Sci. Rep.* **10**, 13308 (2020).

Acknowledgments: We thank the staff of the Materials Research Institute at The Pennsylvania State University for assistance and guidance with material characterization and analysis. **Funding:** This work was supported in part by the National Key Research and Development Program of China (2024YFA1107800), Foundation of Muyuan Laboratory (program ID: 13166022401), and US National Institutes of Health grants (R01NS123433 and R01HL158204).
Author contributions: Conceptualization: Y.W., J.Y., and S.Y. Data curation: Y.W. Formal analysis: Y.W. Funding acquisition: J.Y. and S.Y. Project administration: J.Y. Software: Y.W. Resources: Y.W., J.Y., and S.Y. Methodology: Y.W. and J.Y. Investigation: Y.W., E.G., S.Y., H.X., and X.T. Visualization: Y.W. and S.Y. Supervision: J.Y. and S.Y. Validation: Y.W. Writing—original draft: Y.W., S.Y., and X.T. Writing—review and editing: Y.W., S.Y., X.T., H.J., and J.Y. **Competing interests:** J.Y. and The Pennsylvania State University have a financial interest in Acuitive Technologies Inc. and Aleo BME Inc. These interests have been reviewed by the University's Institutional and Individual Conflict of Interest Committees and are now being managed by the University. All other authors declare that they have no competing interests. **Data and materials availability:** All data and code needed to evaluate and reproduce the results in the paper are present in the paper and/or the Supplementary Materials.

Submitted 21 August 2025
Accepted 16 December 2025
Published 14 January 2026
10.1126/sciadv.aeb6538